2D longitudinal modeling of heat transfer and fluid flow during multilayered

Simon Morville, Muriel Carin, Patrice Peyre, Myriam Gharbi, Denis Carron, Philippe Le Masson, Rémy Fabbro

2D longitudinal modeling of heat transfer and fluid flow during multilayered DLMD process

Simon Morville[1], Muriel Carin[1], Patrice Peyre[2], Myriam Gharbi[2], Denis Carron[1], Philippe Le Masson[1], Rémy Fabbro[2]

[1] *LIMATB, Université de Bretagne-Sud / UEB, Centre de recherche Ch. Huygens, Rue de Saint Maudé, BP 92116, 56321 Lorient cedex, France*

[2] *PIMM, UMR 8006 CNRS-Arts et Métiers Paris Tech, 151 Boulevard de l'Hôpital, 75013 Paris, France*

Abstract

Derived from laser cladding, the Direct Laser Metal Deposition (DLMD) process is based upon a laser beam – powder – melt pool interaction, and enables the manufacturing of complex 3D shapes much faster than conventional processes. However, the surface finish remains critical, and DLMD parts usually necessitate post-machining steps. Within this context, the focus of our work is to improve the understanding of the phenomena responsible for deleterious surface finish by using numerical simulation. Mass, momentum, and energy conservation equations are solved using COMSOL Multiphysics® in a 2D transient model including filler material with surface tension and thermocapillary effects at the free surface. The dynamic shape of the molten zone is explicitly described by a moving mesh based on an Arbitrary Lagrangian Eulerian method (ALE). This model is used to analyze the influence of the process parameters, such as laser power, scanning speed, and powder feed rate, on the melt pool behavior. The simulations of a single layer and multilayer claddings are presented. The numerical

results are compared with experimental data, in terms of layer height, melt pool length, and depth of penetration, obtained from high speed camera. The experiments are carried out on a widely-used aeronautical alloy (Ti-6Al-4V) using a Nd:YAG laser. The results show that the dilution ratio increases with increasing the laser power and the scanning velocity, or with decreasing the powder feed rate. The final surface finish is then improved.

I. Introduction

Direct Laser Metal deposition process results from rapid prototyping techniques and laser cladding. A powder stream is distributed by a nozzle coaxial to a laser beam moving in the x-direction at a V_s scanning speed (Figure 1). The laser beam creates a melt pool by heating a small area of the substrate. Metallic powder reaches the free surface, making a layer of deposited material. Finally, this procedure is repeated many times, layer-by-layer until the entire object is built. The clad shape and the surface finish depend on the energy absorbed by the substrate, the amount of material deposited and the dynamic of the molten zone (surface tension and Marangoni effect). Therefore, numerical modeling can give real insight into the additive laser process, improving our understanding of the underlying physics occurring in the laser interaction zone and the correlation of the process parameters.

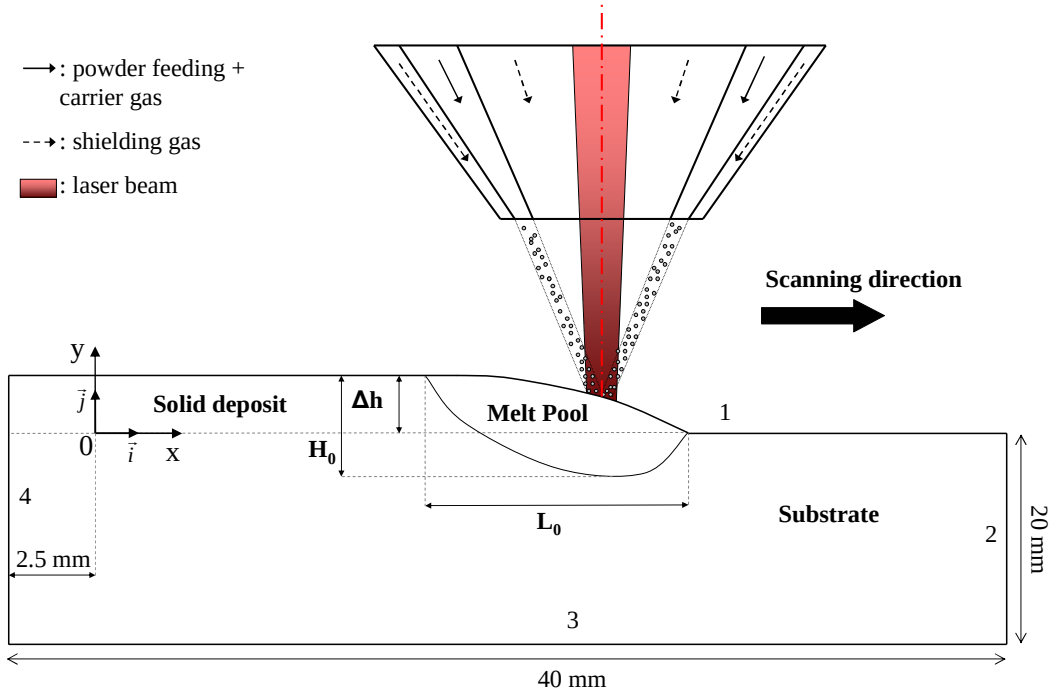

Figure 1 : Observable quantities for DLMD process in a longitudinal section and numbering of the boundaries

Analytical and numerical models have been developed to simulate the DLMD process. Hoadley and Rappaz [1] proposed a thermal model of 2D quasi-stationary laser cladding to determine the temperature field. In their approach, the powder is not supposed to melt instantaneously at the surface but is completely distributed in the liquid prior to melting. This study focuses on the influence of laser power and scanning speed on the dilution and the thickness of the deposit. De Oliveira et al. [2] established correlations between the geometry of the molten zone and the operating parameters from an analytical model and experimental data. Picasso and Hoadley [3] presented a 2D thermal hydrodynamic quasi-stationary model taking into account the surface tension and the Marangoni effect. The position of the free boundary is determined by a force balance and the clad height is computed using mass conservation. Toyserkani et al. [4] proposed a 3D model and solved

the transient heat equation by the finite element method. Hydrodynamic effects are taken into account by means of an effective thermal conductivity in the molten zone. The interaction between powder and melt pool is assumed to be decoupled. The shape of molten zone is deduced from the thermal problem. It is assumed that the layer is deposited on the intersection of the melt pool and the powder stream. The thickness is calculated based on the powder feed rate and elapsed time. A more sophisticated model has been proposed by Han et al. [5]. Their model takes into account heat transfer, phase changes, mass addition, fluid flow, and interactions between the laser beam and the powder flow. To track the liquid/gas interface and simulate the continuous addition of material, the authors used the level-set method. Thus, their 2D model can predict the geometry of the clad and the temperature and velocity fields. In addition, it is able to handle the particle impinging, giving some insight into the mechanisms of the interaction between the powder and melt pool. This approach has also been extended to 3-D equivalent models ([6], [7]). However, most of these models are limited to single layer cladding. Few models deal with multilayer cladding. To simulate the generation of several layers, some authors have used cell activation ([8]) or a specific function for thermal conductivity which depends on time and space to describe the movement of the front ([9]). However, in these works, the fluid flow in the melt pool was neglected, as well as the surface tension and thermocapillary force. A more physically-based model has been recently proposed by Kong and Kovacevik [10]. The authors developed a 2D transient heat transfer and fluid flow model for a multilayer laser cladding process. A level-set method is used to track the evolution of the free surface.

In this paper, a self-consistent 2D transient DLMD model is presented, in which the geometry of single or multilayer clads is calculated as a function of the process parameters (scanning speed, laser energy distribution, powder feed rate). The equations of conservation of energy, mass and momentum are solved in a coupled manner with the finite element software Comsol Multiphysics® v4.2a. The geometry of the deposited layer is explicitly described using an Arbitrary Lagrangian-Eulerian (ALE) moving mesh. It takes into account mass addition, melting and solidification phase changes, surface tension and Marangoni effect. Thermophysical properties, corresponding to the titanium alloy Ti-6Al-4V, depend on temperature in solid and liquid phases.

II. Experimental Procedure

Experiments were carried out with a CW Nd:YAG 8002 TRUMPF disc laser, with a maximum power of 8 kW. The laser beam was delivered through a 200 µm optical fibre, using a collimating and focusing lens that generates a focal spot of 400 µm diameter. A helical powder nozzle was used, where the powder material (45 -75 µm average grain size) is delivered coaxially with the laser beam, resulting in a 4.4 mm powder focus diameter located at the melt pool surface, and with average powder feed rates of 1 - 3 g/min. The spatial concentration profile of powder flow was shown experimentally to have a quasi Gaussian distribution. Argon was used as a carrier and shielding gas, in order to ensure powder conveyance, and to limit oxidation.

The melt pool dynamic was analysed with a CMOS fast camera (PHOTRON IMAGER FASTCAM) with a maximum recording rate of 100 kHz. Lateral observations

of the melt pool were realized by placing this camera on the side, perpendicularly to the scanning displacement.

III. Numerical Simulations

1. Governing Equations

The computational domain is initially composed of a rectangle of 40 x 20 mm (Figure 1). The surrounding gas phase is not modeled because of the large difference of densities and dynamic viscosities between the liquid metal and the gas phase. The model, which uses a Darcy condition to damp the velocity in the solid zone, includes energy conservation equation (1.1), momentum conservation equation (1.2) and mass conservation equation (1.3). It applies to the liquid phase (assumed incompressible Newtonian fluid and laminar flow), the solid phase and the mushy zone:

$$\rho c_p^* \left(\frac{\partial T}{\partial t} + (\vec{u} - \vec{u}_m) \cdot \vec{\nabla} T \right) = \vec{\nabla} \cdot (\lambda \vec{\nabla} T) + Q_v \tag{1.1}$$

$$\rho_0 \left[\frac{\partial \vec{u}}{\partial t} + \left((\vec{u} - \vec{u}_m) \cdot \vec{\nabla} \right) \vec{u} \right] = \vec{\nabla} \cdot \left[-pI + \mu_0 \left(\vec{\nabla} \vec{u} + \left(\vec{\nabla} \vec{u} \right)^T \right) \right] + \vec{F}_{buoyancy} + \vec{F}_{Darcy} \tag{1.2}$$

$$\vec{\nabla} \cdot \vec{u} = 0 \tag{1.3}$$

where ρ is the density (kg.m^{-3}), c_p* is the equivalent heat capacity (J.kg^{-1}.K^{-1}) which is expressed by (1.5), T is the temperature (K), λ is the thermal conductivity (W.m^{-1}.K^{-1}) and Q_v is the heat source (W.m^{-3}). ρ_0 is the density at $T = T_m$, $\vec{u}$ is the fluid velocity vector (m.s^{-1}), $\vec{u}_m$ is the mesh velocity vector (m.s^{-1}), p is the pressure (Pa) and μ_0 is the dynamic viscosity (Pa.s).

As the substrate thickness w_0 is relatively low compared to other dimensions, heat loss in the out-of-plane dimension (z-direction) is modeled via a volumetric sink term Q_v in the energy equation in order to match the experimental configuration as closely as possible. This loss simulates convection and radiation to ambient air occuring at the two large walls of the susbtrate and is expressed as follows:

$$Q_v = -2\frac{\left(h_c\left(T-T_0\right)+\varepsilon\sigma_B\left(T^4-T_0^4\right)\right)}{w_0} \tag{1.4}$$

where h_c is the heat convection coefficient, T_0 is the ambient temperature, ε is the emissivity and σ_B is the Stefan-Boltzmann constant.

The equivalent heat capacity is:

$$c_p^* = c_p\left(T\right)+\frac{\Delta H_m}{\sqrt{\pi\left(T_L-T_S\right)^2}}\exp\left(-\frac{\left(T-T_m\right)^2}{\left(T_L-T_S\right)^2}\right) \tag{1.5}$$

where T_m is the temperature at the melting point (K), defined by the mean temperature between T_L and T_S, the liquidus and solidus temperatures (K) respectively and ΔH_m is the latent heat of fusion (J.kg^{-1}).

The last two terms in (1.2) represent the buoyancy forces and Darcy term. The buoyancy forces are due to density gradients associated with expansion of the liquid metal and are usually expressed using the Boussinesq approximation, as follows:

$$\vec{F}_{buoyancy} = \rho_0\left(1-\beta\left(T-T_m\right)\right)\vec{g} \tag{1.6}$$

The Darcy term represents the damping force when fluid goes through a porous media (dendrite structures). This term is assumed to vary with liquid fraction (1.8) and can be expressed according to the Kozeny-Carman equation [11]:

$$\vec{F}_{Darcy} = -\frac{180\mu_0}{d^2}\frac{(1-f_L)^2}{\left(f_L^{\,3}+\tau\right)}\cdot\left(\vec{u}-\vec{u}_m\right) \tag{1.7}$$

The d parameter is related to the dendrite diameter [12] and τ is a numerical trick to avoid singularity when the liquid fraction is zero (here τ = 0.001).

The liquid fraction f_L is assumed to vary linearly as a function of temperature in the mushy zone delimited by the solidus T_S and liquidus T_L temperatures and is defined as follows:

$$f_L = \begin{cases} 0 & T < T_S \\ \dfrac{T-T_S}{T_L-T_S} & T_S \le T \le T_L \\ 1 & T_L < T \end{cases} \tag{1.8}$$

2. Initial & Boundary Conditions

Table 1 : Boundary conditions (see Figure 1 for the boundary numbers)

N#	1	2, 3, 4
Heat transfer	$\lambda\cdot\vec{\nabla}T\cdot\vec{n} = I_0$ $-h_c\left(T-T_0\right)$ $-\varepsilon\sigma\left(T^4-T_0^4\right)$ $-\rho\, c_P^*\,\vec{V}_P\cdot\vec{n}\left(T-T_P\right)$	$\lambda\vec{\nabla}T\cdot\vec{n} =$ $-h_c\left(T-T_0\right)$ $-\varepsilon\sigma_B\left(T^4-T_0^4\right)$
Fluid	Normal direction: $\sigma\cdot\vec{n} = -\kappa\,\gamma\cdot\vec{n}$ Tangential direction: $\sigma_t = \dfrac{\partial\gamma}{\partial T}\vec{\nabla}T\cdot\vec{t}$	$\vec{u} = \vec{0}$
Moving mesh	$V_n = \vec{u}\cdot\vec{n} + \vec{V}_p\cdot\vec{n}$	$V_n = 0$

The substrate is assumed to be initially at the ambient temperature T_0, and the initial velocity field and initial pressure field at a zero value. For the thermal problem, the boundary conditions take into account the laser source, convection and radiation losses. They are specified in Table 1. All material properties and model parameters are summarised in Table 2 (see Boivineau et al. [13] concerning temperature dependent properties).

The energy distribution intensity I_0 (W.m^{-2}) is considered as uniform and takes into account the attenuation of the heat flux due to the inclination of the free boundary compared with the incident laser beam.

$$I_0(x,t) = \begin{cases} \dfrac{\alpha \cos(\theta) P_l}{\pi r_l^2} & |x - V_S\, t| \le r_l \\ 0 & |x - V_S\, t| > r_l \end{cases} \tag{1.9}$$

with α the absorptivity of the material, θ the incidence angle, P_l the incident laser power, r_l the laser beam radius and V_S the laser beam velocity.

Although models of beam attenuation have been developed (Pinkerton [20]), the attenuation of the laser beam by the powder particles is not accounted for in this model. In fact, a part of the laser beam energy is absorbed by the powder particles, but this energy is redistributed when the particles fall into the melt pool. Moreover, the powder particles are supposed to be at the same temperature as the melt pool ($T_p = T$). Note that the energy required to melt the powder particles represent less than 10% of the laser power.

V_p represents the boundary moving velocity due to powder addition. Momentum quantity associated with the material addition in the molten zone is neglected. The calculation of V_p is given by:

$$\vec{V}_p = N_p \frac{\eta_p D_m}{\rho_0 \pi r_p^2} \exp\left(-N_p \frac{(x - V_S t)^2}{r_p^2} \right) \cdot \vec{j} \quad (1.10)$$

N_p and r_p are respectively the constriction coefficient and the standard deviation of the gaussian distribution. They have been determined by a local measurement of powder flow in different locations of the powder focal plane. The powder catchment efficiency is expressed through η_p. It is calculated by assessing the mass difference between the deposited material and the quantity of powder delivered by the nozzle during a given period. ρ_0 is the powder density at $T = T_m$. Note that V_p is considered equal to zero when the surface temperature is below the melting point.

Table 2 : Material properties and parameters used in the calculations

Initial temperature	T_0 (K)	293
Solidus temperature	T_S (K)	1873 [13]
Liquidus temperature	T_L (K)	1923 [13]
Thermal conductivity	λ (W.m^{-1}.K^{-1})	[13]
Specific heat capacity	c_p (J.kg^{-1}.K^{-1})	[13]
Density	ρ (kg.m^{-3})	[13]
Convection coefficient	h_c (W.m^{-2}.K^{-1})	[20] *
Emissivity	ε	0.4 [13]
Absorptivity	α	0.4 [13]
Stefan -Boltzmann constant	σ_B (W.m^{-2}.K^{-4})	5.67×10^{-8}

Latent heat of fusion	ΔH_m (J.kg^{-1})	3×10^5 [13]
Surface tension coefficient	γ (N.m^{-1})	1.5 [14] [15]
Thermocapillary coefficient	$\partial\gamma/\partial T$ (N.m^{-1}.K^{-1})	-2.7×10^{-4} [16][17]
Laser power	P_l (W)	320 to 500
Laser beam radius	r_l (mm)	0.65
Mass powder rate	D_m (g.min^{-1})	1 to 2
Powder stream radius	r_p (mm)	2.2
Constriction coefficient	N_p	5
Powder catchment efficiency	η_p	0.5
Scanning speed	V_S (m.min^{-1})	0.1 to 0.4
Reference liquid density	ρ_0 (kg.m^{-3})	3800 at $T=T_L$ [13]
Dynamic viscosity	μ_0 (Pa.s)	4×10^{-3}
Thermal expansion coefficient	β (K^{-1})	2×10^{-4}
Substrate thickness	w_0 (m)	0.002
Dendrite diameter	d (m)	10^{-4}

** The value of convection coeffcient is chosen according to forced convection conditions. Wang and Felicelli have shown that the influence of the convective heat transfer coefficient on the temperature field is moderate for $1 < h_c < 100$ [18]. However, a more realistic value can be found using the approach proposed by Zekovic et al. [19]. They developed a 3D model of the turbulent gas-powder flow, which reveals zones of intense gas flow over the wall surfaces, due to forced convection caused by the powder-gas stream.*

3. Resolution Parameters & Mesh

The moving mesh is managed by the ALE method implemented in Comsol Multiphysics®, with a hyperelastic smoothing method. The resolution is performed with the direct PARDISO solver associated with generalized-α temporal solver. Relative and absolute tolerances are respectively 10^{-3} and 10^{-4}. The mesh consists of 38,676 triangular elements with a maximum size of 20 µm at the boundary 1 (Figure 1). Quadratic elements are chosen for the momentum and moving mesh equations, and linear elements for the energy equation. Simulations are performed on a computing station (24 x 3.33 GHz - 96 GB RAM). Each simulation is performed with four processors. The CPU time ranged from 4 to 5 days for a deposited layer of 35 mm long and about 4 weeks for five layers.

Table 3 : Optimization of the mesh element size

Max. element size at bnd 1	10 µm	20 µm	40 µm
Max. temperature	2239 K	2241 K	2244 K
Max. velocity	0,90 $m.s^{-1}$	0,92 $m.s^{-1}$	1,15 $m.s^{-1}$
CPU time / Degrees of freedom	36,379 s / 255,369	8,360 s / 87,854	3,664 s / 32,517

The spatial convergence is checked by refining the mesh. In order to reduce computation time, these calculations are performed in a moving coordinate system which moves at the same velocity as the heat source. The influence of the mesh element size on the maximum temperature and velocity is presented in Table 3. It can be observed that

the maximum temperature is slightly affected by the mesh refining (less than 1%). However, a 20% improvement is shown in the accuracy of the maximum fluid velocity from 40 µm to 20 µm on the surface, with an increase of 128% on the computation time. The gain is only 2% from 20 µm to 10 µm, while the computing time increases by 335%. Moreover, the influence of the mesh on the quasi-stationary size of the molten zone (length, total height, substrate depth) is small (<2%). A mesh element size of 20 µm is then used for all the computations. Note that the error on the energy conservation remains less than 10% during the five layers deposition modeling, but the accuracy of the model could be improved using local remeshing.

IV. Numerical Results & Discussion

1. Single layer deposition

Figure 2 shows the melt pool shape and the velocity vector field in the melt pool for P_l = 400 W, V_S = 0.4 m.min^{-1} and D_m = 2 g.min^{-1} at t = 2.625 s during a single layer deposition. The thermocapillary coefficient, negative for the Ti-6Al-4V, is driving the flow to the periphery of the molten zone. One can observe the existence of two convective cells nearly stable, the most important being responsible for the melt pool spread on the back.

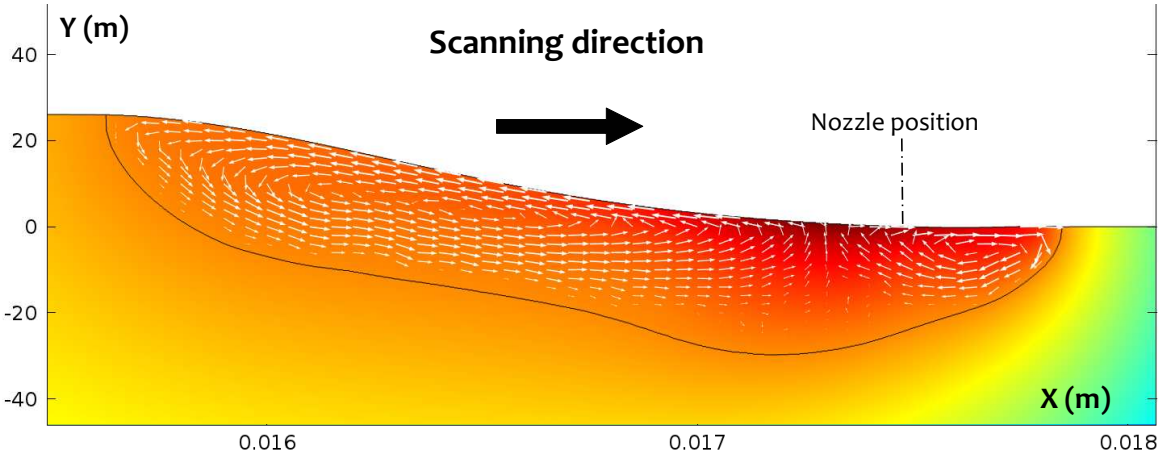

Figure 2 : Fluid flow in the molten pool during DLMD process at t = 2.625 s

(P_l = 400 W, V_S = 0.4 m.min^{-1}, D_m = 2 g.min^{-1})

Temperature and velocity profiles along the boundary 1 are plotted in Figure 3 at t = 2.625 s, which corresponds to a laser beam located at x = 17.5 mm. The maximum temperature at the surface of the melt pool is 2471 K, indicating that no evaporation occurs. On each side of the peak temperature location, thermal gradients are of opposite sign, leading to a fluid flow velocity equal to zero at that point due to Marangoni effect. The thermal gradients become maximal at the edge of the laser beam, which explains the velocity peaks observed.

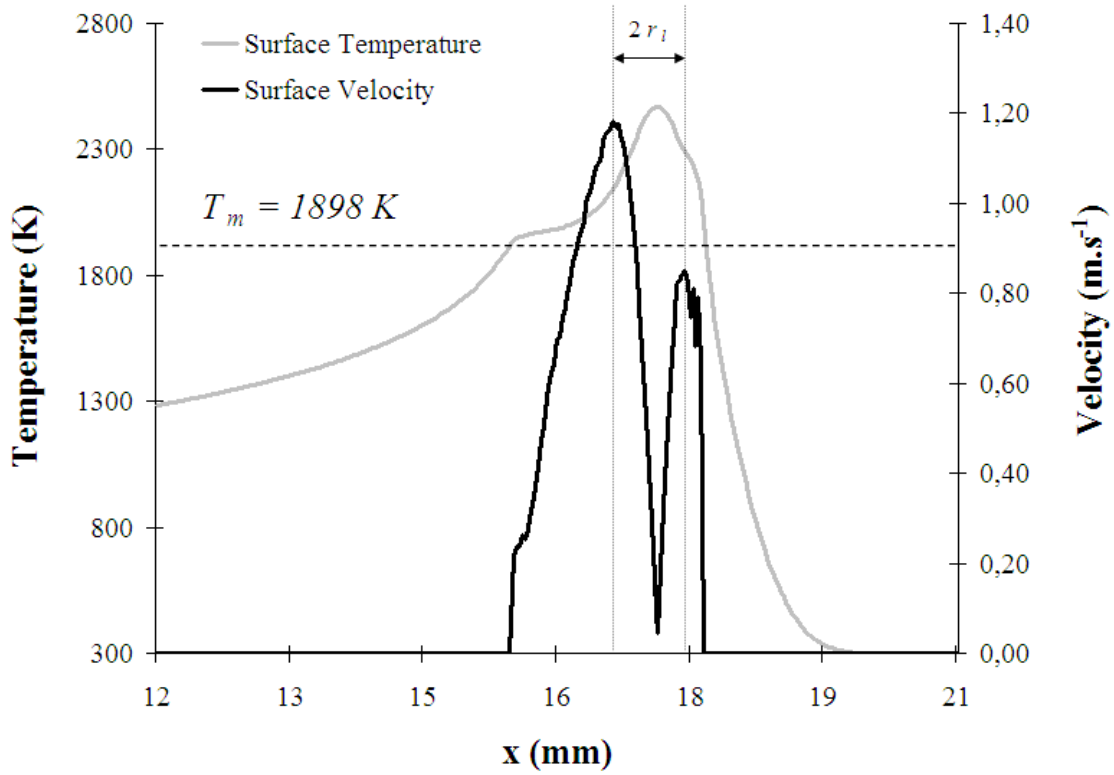

Figure 3 : Temperature and velocity distributions at the substrate surface (P_l = 400 W, V_S = 0.4 m.min^{-1}, D_m = 2 g.min^{-1}) at t = 2.625 s

In order to demonstrate the ability of the model, a series of calculations was performed for a laser power from 320 to 500 W, a scanning speed from 0.1 to 0.4 m.min^{-1} and a powder feed rate of 1 and 2 g.min^{-1}. The evolutions of melt pool length L_0, melt pool height H_0 and deposition height Δh versus the linear energy P_l / V_s are presented in Figure 4. Numerical results are compared with measurements obtained from high speed camera.

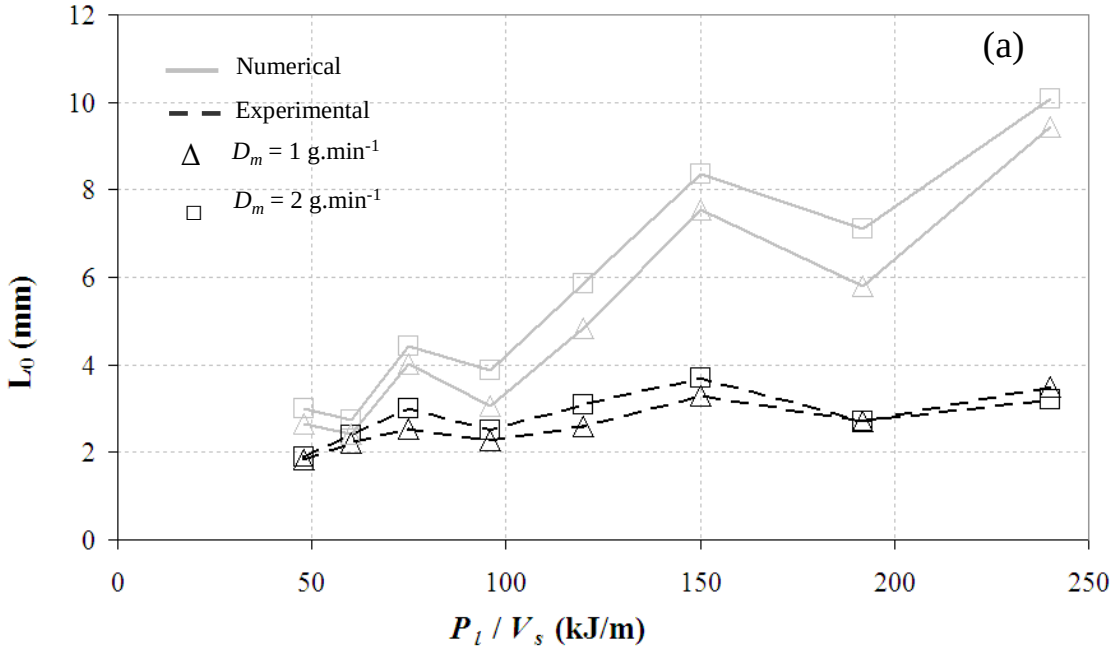
(a)
Numerical
Experimental
D_m = 1 g.min^{-1}
D_m = 2 g.min^{-1}
L_0 (mm)
P_l / V_s (kJ/m)
0
2
4
6
8
10
12
0
50
100
150
200
250

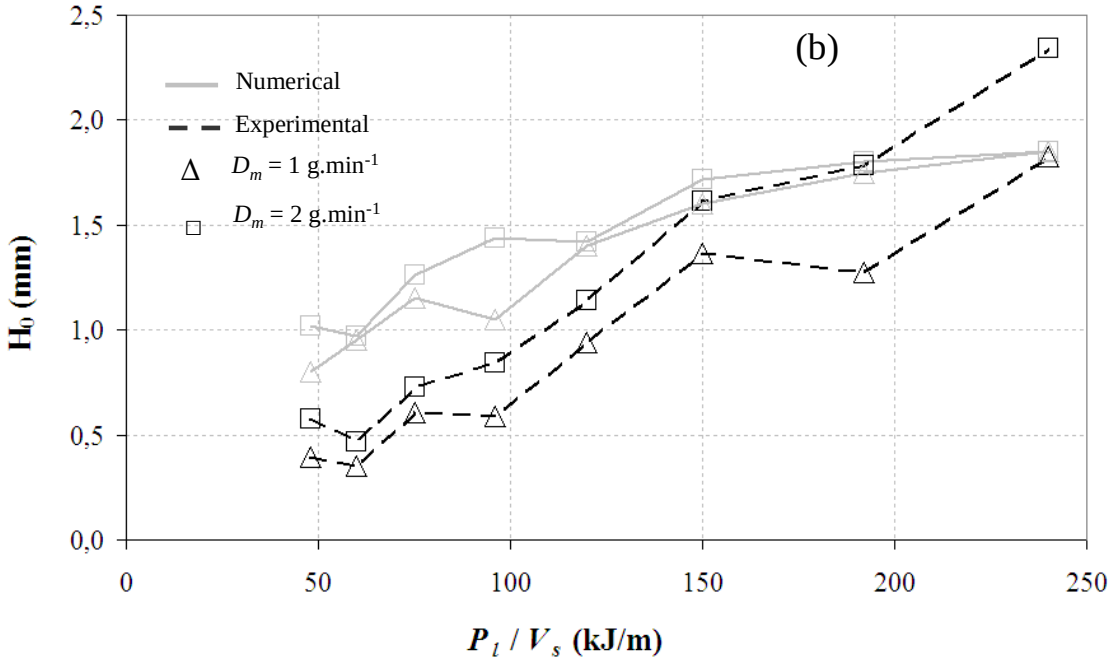
(b)
Numerical
Experimental
D_m = 1 g.min^{-1}
D_m = 2 g.min^{-1}
H_0 (mm)
P_l / V_s (kJ/m)
0,0
0,5
1,0
1,5
2,0
2,5
0
50
100
150
200
250

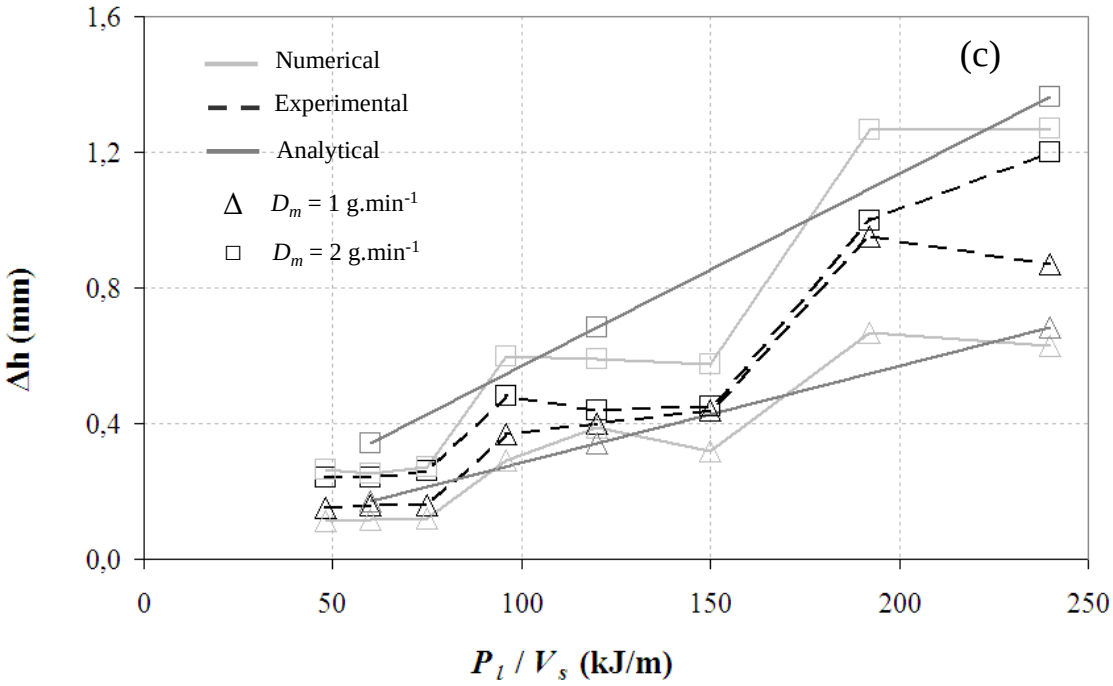

Figure 4 : Comparison of numerical results with measurements for 1 g.min^{-1} and 2 g.min^{-1}: (a) melt pool length, (b) melt pool height, (c) deposition height

The evolutions of the molten zone as a function of linear energy are qualitatively consistent with experimental observations. However, the numerical model overestimates greatly the length of the molten zone. This can be explained by the 2D assumption that neglects the convective motion in the transverse plane (z-direction), responsible for a heat redistribution by the fluid flow.

The theoretical evolution of the deposit height (Figure 4c) is obtained from Equation (1.11), proposed by Fathi et al. [21]. Their model considers a parabolic shape for the clad. The height is assumed to depend on two process parameters which are the scanning speed and powder feed rate and is given by:

$$\Delta h = \frac{3 \cdot \eta_P \cdot D_m}{2 \cdot \rho \cdot w_0 \cdot V_S} \tag{1.11}$$

with w_0 the width of the substrate. Analytical values are in good agreement both with numerical results and measurements. The calculated melt pool behavior regarding to process parameters is also consistent with literature data ([2][21]).

2. Improvement of Surface Finish

One of the current limitations in Direct Laser Metal Deposition process is the final surface finish, which requires a post machining step to satisfy quality standard. Indeed, the multilayered depositions generate a stepped lateral surface. The curvature of each track results in a rough lateral surface, as shown in Figure 5. In order to identify the process parameters responsible for the surface degradation during DLMD process, Gharbi et al. [22] have realized multilayered walls by varying the laser power, the mass powder rate and the scanning speed. In this work, the size of the melt pool is measured using a fast camera and the surface finish is quantified by measuring the W_t parameter using a profilometer. This parameter represents the maximum “peak-to-valley” waviness and is defined in Figure 5a. The surface finish is then better when the W_t parameter is small.

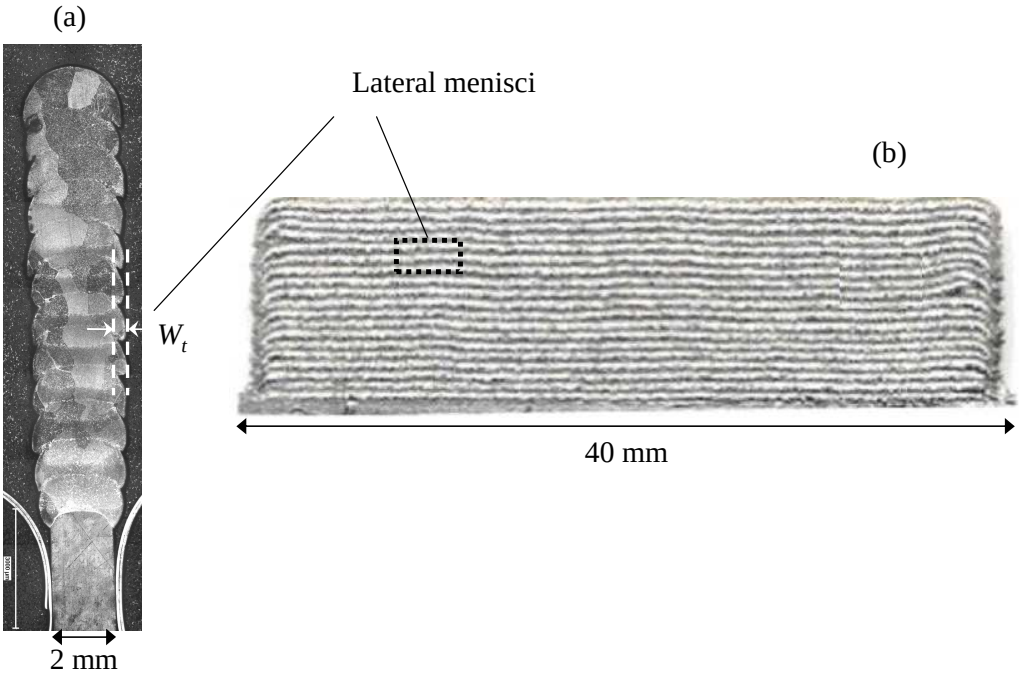

Figure 5 : Macrographs of a deposited thin wall : (a) cross-section view,

(b) longitudinal view

It has been shown that a reduction of layer thickness and an increase of melt pool size have a beneficial effect on the surface finish. The experimental data have been used to identify a correlation between the W_t parameter and the dilution ratio, which is defined by:

$$D = \frac{\left(H_0 - \Delta h\right)}{H_0} \tag{1.12}$$

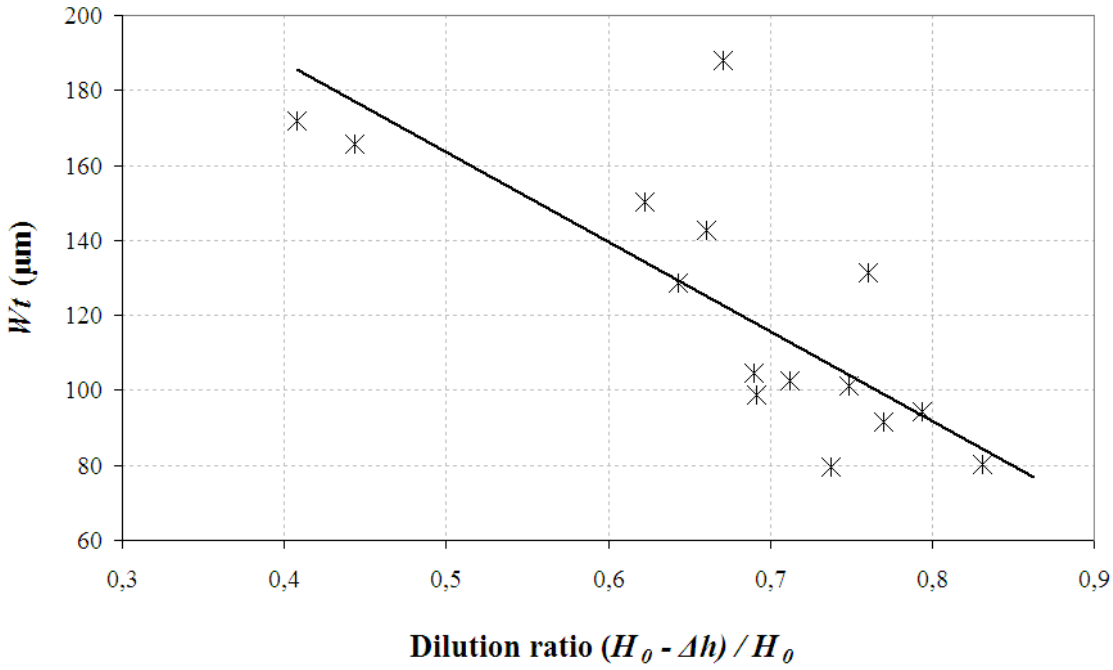

Figure 6 : Measured W_t parameter as a function of dilution

Figure 6 shows the decrease of the measured W_t parameter with the dilution obtained by varying the laser power (320 – 500 W), the scanning speed (0.1 – 0.4 m.min^{-1}) and powder feed rate (1 – 2 g.min^{-1}). Based on the correlation between the dilution and the surface finish, the 2D model has been used to identify the process parameters leading to large dilution and thus a better surface finish. Figures 7 and 8 present the evolution of the dilution as a function of linear energy (P_l / V_s) and linear mass (D_m / V_s) respectively. For a linear energy less than 250 kJ.m^{-1}, the model predicts the same trends as those observed experimentally. For a given scanning velocity, the dilution is larger for high laser power and low powder feed rate. Increasing the scanning velocity also improves the dilution in all cases. Therefore, a better surface finish is obtained with high laser power, high scanning speed and low powder feed rate. For a linear energy higher than 250 kJ.m^{-1} (for example, P_l = 500 W, V_S = 0.1 m.min^{-1}), the discrepancy between experimental and

numerical results increases drastically due to the 2D assumption. The corresponding results are not reported in Figures 7 and 8. These results are also in agreement with the experimental results obtained by Unocic and DuPont [23]. For the case of one layer deposed on a substrate, it is shown that dilution ratio increases with increasing laser power and scanning velocity and decreasing powder mass flow rate. However the surface finish is not studied in this work.

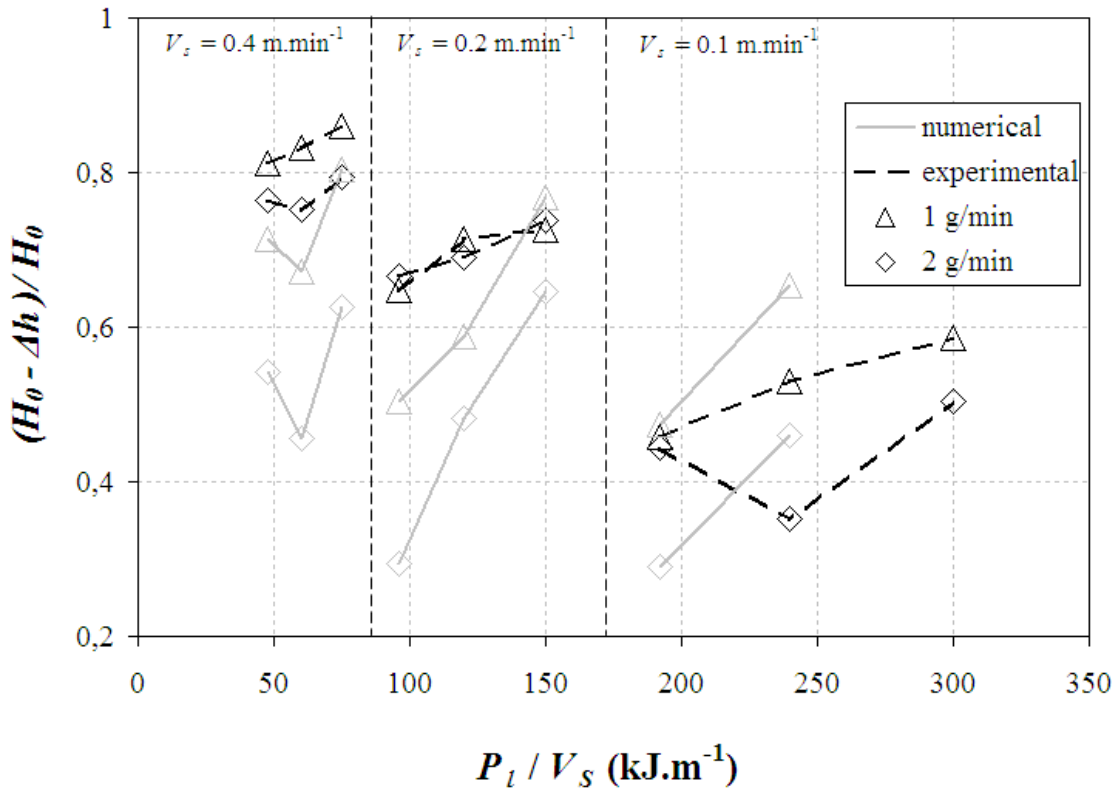

Figure 7 : Dilution versus linear energy

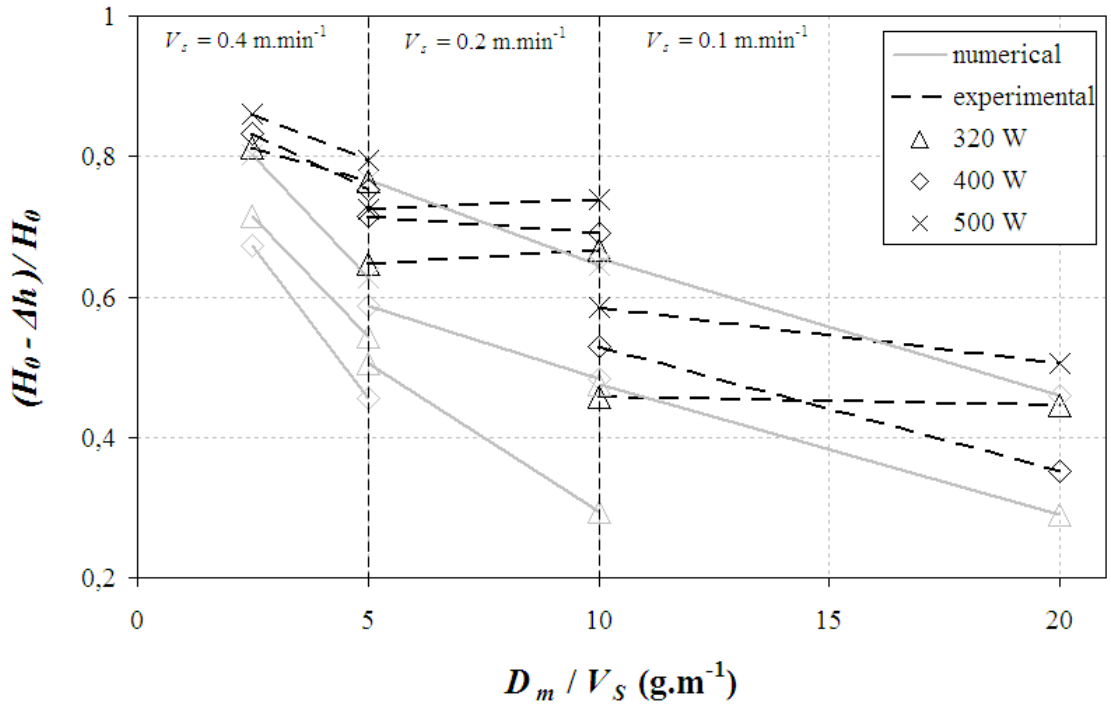

Figure 8 : Dilution versus linear mass

The influence of process parameters on the surface finish has been studied in a limited number of works. Alimardani et al. [24] recently shows that for a given powder feed rate the smoothness and the uniformity of a deposit wall were enhanced by increasing the scanning velocity, which reduces the thickness of the individual layer. Moreover it is shown that the laser power has to be increased with scanning speed to keep a good surface finish. Yakovlev et al. [25] insist on the influence of scanning velocity, power density and powder feed rate that determine whether a deposited layer is smooth and continuous or degraded.

3. Multilayer Deposition

In this section, a five-layer laser deposition manufacturing process is simulated. Each layer is carried out according to a nozzle displacement from x = 0 mm to x = 35 mm for the five layers, with 20 s idle time before starting the next layer. The process parameters are P_l = 400 W, V_S = 0.4 m.min^{-1} and D_m = 2 g.min^{-1}. With this scanning speed, the five layers are achieved in 106.25 s. The total height is 1.37 mm.

Figure 9 presents the evolution of the melt pool dimensions during the first to fifth layers. Figure 10 shows the shape of the melt pool for the 1st, 3rd and 5th layers. It can be observed that the melt pool size increases as the wall height rises, as shown in Figure 9. Between the 1st and 5th layer, the length L_0, the whole height H_0 and the deposit height Δh of the melt pool are respectively increased by 16%, 15% and 12%. The increase of the melt pool size is attributed to the storage of energy into the wall during the deposition of successive layers.

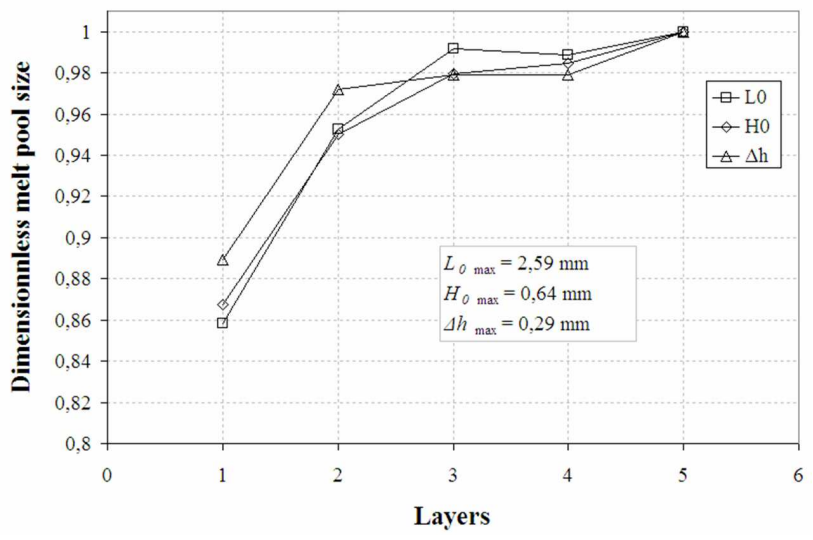

Figure 9 : Evolution of the melt pool dimensions during the deposition of the first to fifth layers

This is confirmed by the evolution of peak temperature at the melt pool surface and the temperature of a point in the substrate (Figure 11). During the deposition of the first layer, the temperature of the substrate increases as the laser approaches, then decreases as the laser reaches the end of the wall. The temperature continuously reduces during the idle time of 20 s. During the next layers, the substrate temperature exhibits a periodic evolution with increasing maximum and minimum, except for the fourth and fifth layers. The maximum temperature of the substrate begins to reduce with increasing distance from the melt pool.

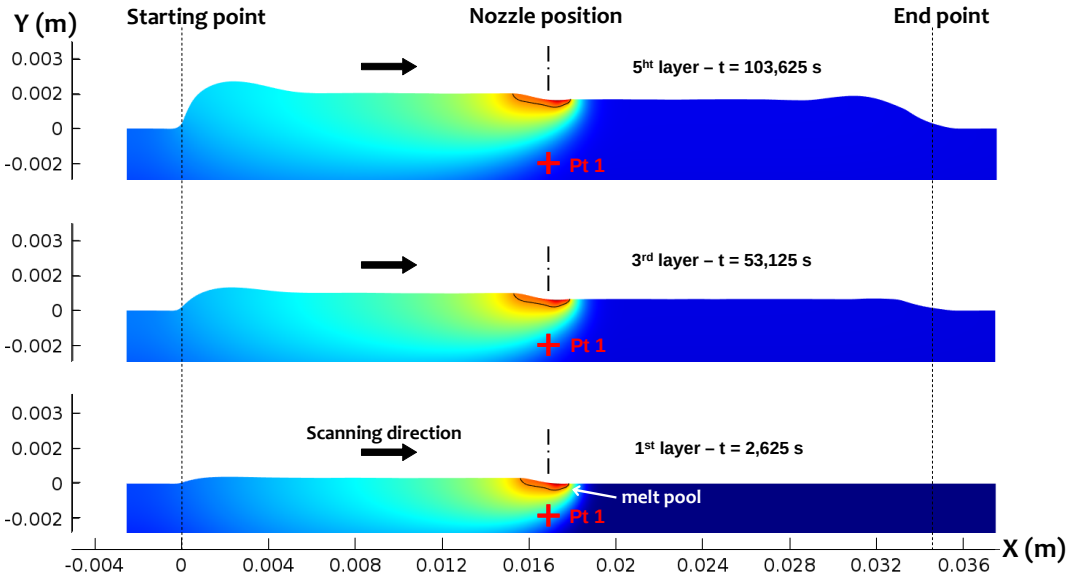

Figure 10 : Temperature field and melt pool shape for the 1st, 3rd and 5th layers

After the deposition of five layers, it can be observed in Figure 10 an increase of the clad height at the two end-points of each layer. This phenomena has already been observed numerically and experimentally by Alimardani et al. [26]. To better understand

this increase, Figure 12 shows the temperature field and the melt pool shape at different times obtained for the fifth layer. It can be observed that at the beginning of a layer, the melt pool length is very small (Figure 12 a), so the amount of metallic powder is spread over a reduced area. The resulting deposit height is then larger. As the laser is moving, the melt pool length increases due to edge effects. At the extremity of the wall, the heat diffusion directions are reduced and the peak temperature at the surface of the melt pool rises. The thermal gradients become higher leading to larger fluid velocities at the melt pool surface due to Marangoni effect. The added material is then ejected at the rear of the melt pool which contributes to increase the height of the layer at the extremity (Figure 12 b). As the melt pool is moving, the melt pool length tends to diminish and reaches a stable value leading to a constant clad height (Figure 12 c). When the nozzle reaches the end of the wall, the melt pool length begins again to increase due to edge effect and then decreases at the extremity of the wall (Figure 12 d). The fluid flow drives the material at the rear of the melt pool inducing an excess of material at this extremity. The increase of clad height is less pronounced than that observed at the extremity located at $x = 0$, because of the scan strategy of the nozzle, which always moves in the same direction. The rounded shape observed at the two end-points of the wall can be attributed to the surface tension effect. This typical shape can not be predicted by purely conductive models, as the one proposed by Alimardani et al. [26]. Their comparison between experimental and numerical results shows that their model can not reproduce the experimental shapes observed at the two end-points.

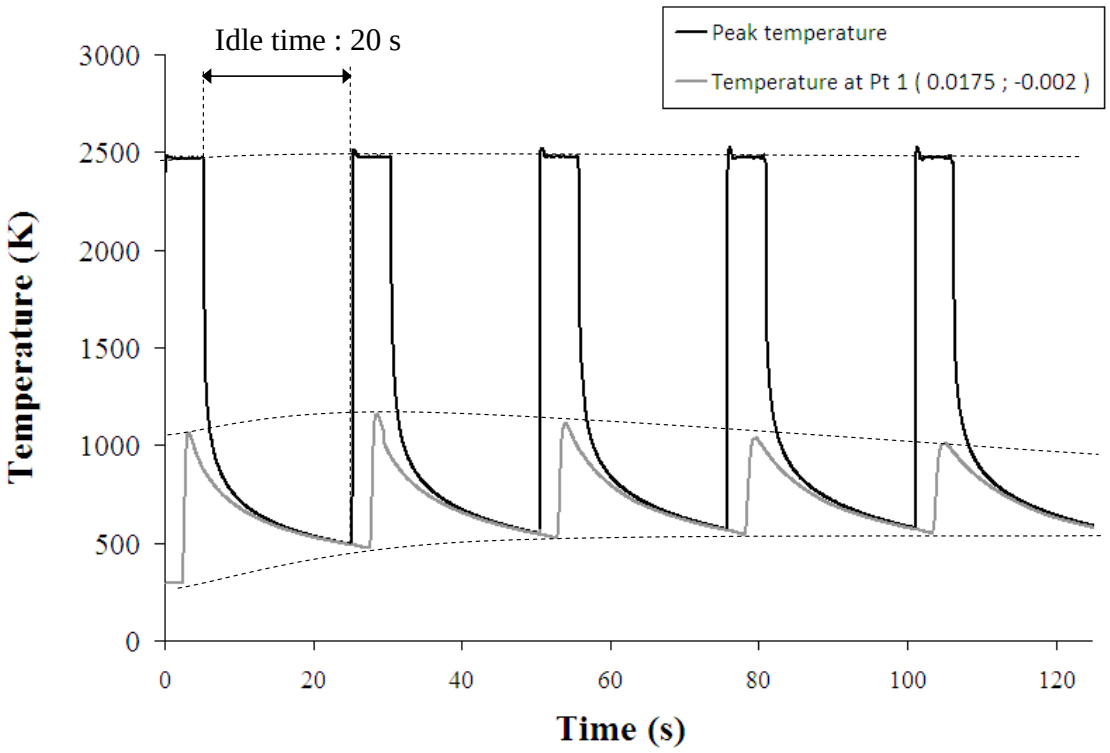

Figure 11 : Evolution of the peak temperature and temperature of one point Pt 1 (0.0175, -0.002) in the substrate (see Figure 10) during the deposition of the first to fifth layers

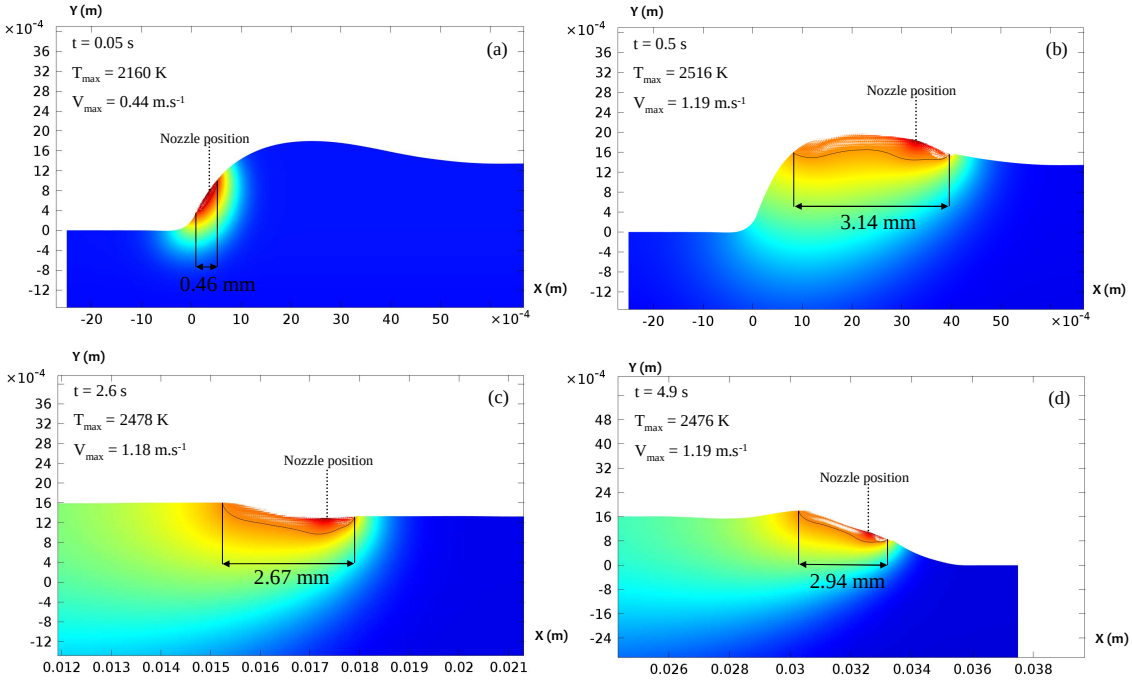

Figure 12 : Temperature field and melt pool shape at different times during the deposition of the fifth layer

V. Summary and conclusion

A self-consistent 2D transient heat transfer and fluid flow model has been developped for simulating a multilayered direct metal laser deposition process. The main physical phenomena are taken into account, such as surface tension effect and addition of powder. The dynamic shape of the free surface is explicitly tracked by using an ALE moving mesh. A numerical analysis shows the dependencies between the geometry of the molten zone and the primary operating parameters (laser power, scanning speed, powder feed rate). Experimental results indicate that the surface finish is improved with high dilution ratio, which corresponds to a small thickness of each layer. The 2D model is used to identify the process parameters resulting in high dilution ratio and thus a better surface finish. It is demonstrated that dilution ratio increases with increasing laser power and

scanning velocity and decreasing powder feed rate. The deposition of five layers is successfully simulated. It is observed an increase of the melt pool size during the deposition of the five layers. The shape of the different layers is analysed. The increase of the clad height at the two end-points of the wall is attributed to thermal phenomenon due to edge effect combined with Marangoni effect. The comparison between experimental and numerical results has indicated that the melt pool height and the layer thickness are well predicted by the model but the melt pool length appears to be largely overestimated by the model. This discrepancy has been attributed to the 2D assumption which neglects transverse fluid flow. In the future, a 3D heat transfer and fluid flow model will be developped in order to obtain more realistic results which are comparable to the corresponding experiments.

Acknowledgements

This work is supported by French Agency for Research (ANR) under the ASPECT project referenced ANR-09-BLAN-0014-02.

References

[1] Hoadley, A.F.A., Rappaz, M., (1992), A thermal model of laser cladding by powder injection, Metallurgical Transactions B. 23, 631-642

[2] De Oliveira, U., Ocelik, V., De Hosson, J.T.M., (2005), Analysis of coaxial laser cladding processing conditions, Surface and Coatings Technology 197, 127–136

[3] Picasso, M., Hoadley, A.F.A., (1994), Finite element simulation of laser surface treatments including convection in the melt pool, International Journal of Numerical Methods for Heat & Fluid Flow 4, 61-83

[4] Toyserkani, E., Khajepour, A., Corbin, S. (2004), 3-D finite element modeling of laser cladding by powder injection: effects of laser pulse shaping on the process, Optics and Lasers in Engineering 41, 849-867

[5] Han, L., Phatak, K., Liou, F., (2004), Modeling of laser cladding with powder injection, Metallurgical and Materials Transactions B 35, 1139-1150

[6] Kumar, A., Roy, S., (2009), Effect of three-dimensional melt pool convection on process characteristics during laser cladding, Computational Materials Science 46, 495-506

[7] Wen, S., Shin, Y.C., (2010), Modeling of transport phenomena during the coaxial laser direct deposition process, Journal applied of Physics 108, 044908

[8] Neela, V., De, A., (2009), Three-dimensional heat transfer analysis of LENS^{TM} process using finite element method, International Journal of Advanced Manufacturing Technology 45, 935-943

[9] Peyre, P., Aubry, P., Fabbro, R., Neveu, R., Longuet, A., (2008), Analytical and numerical modelling of the direct metal deposition laser process, Journal of Physics D: Applied Physics 41, 025403

[10] Kong, F., Kovacevic, R., (2010), Modeling of heat transfer and fluid flow in the laser multilayered cladding process, Metallurgical and Materials Transactions B 41, 1310-1320

[11] Brent, A.D., Voller, V.R., Reid, K.J., (1988), Enthalpy–porosity technique for modeling convection–diffusion phase change: application to the melting of a pure metal, Numerical Heat Transfer, Part B: Fundamentals: An International Journal of Computation and Methodology 13, 297

[12] Beckermann, C., Viskanta, R., (1988), Double-diffusive convection during dendritic solidification of a binary mixture, PhysicoChemical Hydrodynamics 10, 195–213

[13] Boivineau, M., Cagran, C., Doytier, D., Eyraud, V., Nadal, M.-H., Wilthan, B., (2006), Thermophysical properties of solid and liquid Ti-6Al-4V (TA6V) alloy, International Journal of Thermophysics 27, 507-529

[14] Wunderlich, R.K., Battezzati, L., Brooks, R., Egry, I., Fecht, H.-J., Garandet, J.-P., (2005), Surface tension and viscosity of industrial alloys from parabolic flight experiments — Results of the ThermoLab project, Microgravity Science Technology 16, 11-14

[15] Vinet, B., Garandet, J.P., Marie, B., Domergue, L., Drevet, B., (2004), Surface tension measurements on industrial alloys by the drop-weight method, International Journal of Thermophysics 25, 869–883

[16] Rai, R., Burgardt, P., Milewski, J.O., Lienert, T.J., DebRoy, T., (2009), Heat transfer and fluid flow during electron beam welding of 21Cr–6Ni–9Mn steel and Ti–6Al–4V alloy, Journal of Physics D: Applied Physics 42, 025503

[17] Meng, T., Factors influencing the fluid flow and heat transfer in electron beam melting of Ti-6Al-4V, (2010)

[18] Wang, L., Felicelli, S., (2006), Analysis of thermal phenomena in LENS(TM) deposition, Materials Science and Engineering: A. 435-436 625-631

[19] Zekovic, S., Dwivedi, R., Kovacevic, R., (2007), Numerical simulation and experimental investigation of gas-powder flow from radially symmetrical nozzles in laser-based direct metal deposition, International Journal of Machine Tools and Manufacture 47, 112-123

[20] Pinkerton, A.J., (2007), An analytical model of beam attenuation and powder heating during coaxial laser direct metal deposition, Journal of Physics D: Applied Physics 40, 7323-7334

[21] Fathi, A., Toyserkani, E., Khajepour, A., Durali, M., (2006), Prediction of melt pool depth and dilution in laser powder deposition, Journal of Physics D: Applied Physics 39, 2613-2623

[22] Gharbi, M., Peyre, P., Gorny, C., Fabbro, R., Morville, S., Carin, M., Malot T., (2011), Influence of process conditions on surface finishes obtained with the direct metal deposition laser technique , proc. ICALEO conference, October 23-27, Orlando, Florida, United States, 687–694.

[23] Unocic, R. R., DuPont, J., (2003), Composition control in the direct laser-deposition process, Metallurgical and Materials Transactions B 34, 439-445

[24] Alimardani, M., Fallah, V., Iravani-Tabrizipour, M., Khajepour, A., (2012), Surface finish in laser solid freeform fabrication of an AISI 303L stainless steel thin wall , Journal of Materials Processing Technology, vol. 212, n^{o}. 1, 113–119

[25] Yakovlev, A., Trunova, E., Grevey, D., Pilloz, M., Smurov, I., (2005), Laser-assisted direct manufacturing of functionally graded 3D objects , Surface and Coatings Technology, vol. 190, n^{o}. 1, 15–24

[26] Alimardani, M., Toyserkani, E., Huissoon, J. P., (2007), A 3D dynamic numerical approach for temperature and thermal stress distributions in multilayer laser solid freeform fabrication process , Optics and Lasers in Engineering, vol. 45, n^{o}. 12, 1115–1130